UNIVERSITY OF WEST BOHEMIA

Applied and Computational Mechanics 4 (2010) 133–142

Applied and Computational Mechanics

Numerical solution of gas exhaustion from a reciprocating engine

M. Žaloudek[a,b,*], J. Fořt[a], H. Deconinck[b]

[a] *Department of Technical Mathematics, Faculty of Mechanical Engineering, Czech Technical University in Prague, Karlovo náměstí 13, 121 35 Praha 2, Czech Republic*

[b] *von Kármán Institute for Fluid Dynamics, Chaussée de Waterloo 72, 1640 Rhode-Saint-Genèse, Belgium*

Received 29 April 2010; received in revised form 5 July 2010

Abstract

This paper presents the numerical simulations of a flow around an exhaust valve, inside the cylinder of a four-stroke combustion engine. The different flow models have been tested. Besides, the impact of the dimensionality and geometry detailness has been studied. Fixed (i.e. non-moving) geometry and steady boundary conditions have been assumed for all simulations. All the results presented have been obtained by a newly developed CFD package, based on finite volume method (FVM) with an AUSM-family numerical scheme.

Keywords: exhaust systems, numerical simulation, finite volume method

1. Introduction

The exhaustion phase in a four-stroke engine is a phenomenon determined by many factors. Except the challenging shape of the exhaust channel inside a real engine, the gas leaves the combustion chamber at supersonic velocity and probably some chemical reactions are still being terminated even during the exhaustion. Whole process is unsteady since at operating engine revolutions the exhaust valve needs to open and close several ten-times per second.

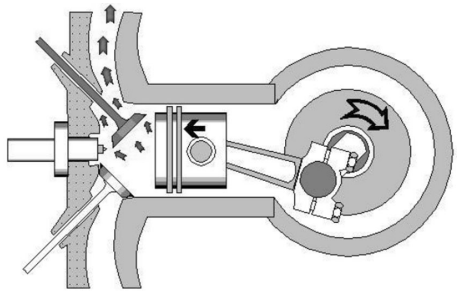

Fig. 1. Reciprocating engine at exhaustion phase, illustrative figure

Due to the tough accessibility to the domain, there are almost no experimental data to compare the numerical solutions with. On top, the vicinity of the exhaust valve belongs to one of the least explored domains in whole engine. Therefore a new numerical software is developed in a stepwise manner, such that we have good confidence in its results as well as in the flow structure during the exhaustion.

*Corresponding author. Tel.: +420 224 357 439, e-mail: Milan.Zaloudek@fs.cvut.cz.

2. Governing Equations

The flow is modelled by conservation laws of mass, momentum and energy in a form

$$\frac{\partial \mathbf{W}}{\partial t} + \frac{\partial \mathbf{F}}{\partial x_1} + \frac{\partial \mathbf{G}}{\partial x_2} + \frac{\partial \mathbf{H}}{\partial x_3} = \frac{\partial \mathbf{R}}{\partial x_1} + \frac{\partial \mathbf{S}}{\partial x_2} + \frac{\partial \mathbf{T}}{\partial x_3}\,, \tag{1}$$

with $\mathbf{W}$ the vector of conservative variables

$$\mathbf{W} \;=\; \left|\rho\,,\, \rho w_1\,,\, \rho w_2\,,\, \rho w_3\,,\, e\right|^T, \tag{2}$$

$\mathbf{F}$, $\mathbf{G}$, $\mathbf{H}$ the convective fluxes and $\mathbf{R}$, $\mathbf{S}$, $\mathbf{T}$ the viscous fluxes

$$\begin{aligned}
\mathbf{F} &= \left|\rho w_1,\, \rho w_1^2 + p,\, \rho w_1 w_2,\, \rho w_1 w_3,\, (e+p)\cdot w_1\right|^T \\
\mathbf{G} &= \left|\rho w_2,\, \rho w_1 w_2,\, \rho w_2^2 + p,\, \rho w_2 w_3,\, (e+p)\cdot w_2\right|^T \\
\mathbf{H} &= \left|\rho w_3,\, \rho w_1 w_3,\, \rho w_2 w_3,\, \rho w_3^2 + p,\, (e+p)\cdot w_3\right|^T \\
\mathbf{R} &= \left|0,\, \tau_{11},\, \tau_{12},\, \tau_{13},\, w_1\tau_{11} + w_2\tau_{12} + w_3\tau_{13} - q_1\right|^T \\
\mathbf{S} &= \left|0,\, \tau_{12},\, \tau_{22},\, \tau_{23},\, w_1\tau_{12} + w_2\tau_{22} + w_3\tau_{23} - q_2\right|^T \\
\mathbf{T} &= \left|0,\, \tau_{13},\, \tau_{23},\, \tau_{33},\, w_1\tau_{13} + w_2\tau_{23} + w_3\tau_{33} - q_3\right|^T .
\end{aligned} \tag{3}$$

The variables ρ, $\vec{w} = (w_1,\, w_2,\, w_3)$, e, p, $h = e + \frac{p}{\rho}$ represent the density, the velocity components, the internal energy per unit volume, the pressure and the enthalpy. The stress tensor τ is considered symmetric, with

$$\tau_{ij} = \begin{cases} \mu\left(2\frac{\partial w_i}{\partial x_j} - \frac{2}{3}\mathrm{div}\,\vec{w}\right) & \text{if } i = j, \\ \mu\left(\frac{\partial w_i}{\partial x_j} + \frac{\partial w_j}{\partial x_i}\right) & \text{if } i \neq j \end{cases} \tag{4}$$

and the heat flux

$$q_i = -\frac{\lambda}{\mathrm{Pr}}\frac{\partial T}{\partial x_i}\,, \tag{5}$$

with λ being the thermal conductivity, Pr the Prandtl number and T the temperature. The system is closed by the equation of state

$$p = (\gamma - 1)\left[e - \frac{1}{2}\rho\left(w_1^2 + w_2^2 + w_3^2\right)\right] \tag{6}$$

and the Sutherland's law

$$\mu = \frac{C_1 T^{3/2}}{T + S}\,, \tag{7}$$

with $\gamma = 1.4$ the Poisson's constant and $C_1 = 1.458 \cdot 10^{-6}\,\frac{\mathrm{kg}}{\mathrm{m\cdot s\cdot\sqrt{K}}}$, $S = 110.4\,\mathrm{K}$ other constitutive air constants. As intimated, the working medium has been considered air respecting the laws of an ideal gas and with no chemistry involved.

Turbulence Model

When turbulent computations mentioned, the two-equation Menter's baseline model [2] is always considered. The model uses a decomposition of flow variables into a mean value and a fluctuation, written as

$$X = \bar{X} + x'. \tag{8}$$

The original equations (1) are understood as the transport equations of actual values. For the set of equations used, Favre's density weighted averaging [1] has been chosen, as it is the suitable averaging for compressible models.

On the right hand side of the momentum equations a tensor of turbulent stresses $\overline{\rho w_i' w_j'}$ occurs due to the averaging. This tensor has been approximated with the Boussinesq hypothesis that assumes analogy between the molecular and the turbulent momentum transport. The tensor is then expressed as

$$-\overline{\rho w_i' w_j'} = \mu_t \left(\frac{\partial \bar{W}_i}{\partial x_j} + \frac{\partial \bar{W}_j}{\partial x_i} - \frac{2}{3}\delta_{ij} \frac{\partial \bar{W}_k}{\partial x_k} \right) - \frac{1}{3}\delta_{ij} \overline{\rho w_k' w_k'}, \tag{9}$$

where the turbulent viscosity μ_t replaces all the unknown entries of the tensor. Such set of averaged equations (so-called Reynolds-Averaged Navier-Stokes equations) holds the form of (1), with the variable τ from equation (3) substituted by summation of terms (4) and (9). The turbulent viscosity is computed as follows

$$\mu_t = \gamma^* \bar{\rho} \frac{k}{\omega}, \tag{10}$$

where γ^* is the model constant, k is the turbulent kinetic energy and ω is the specific dissipation rate. The variables k and ω are computed using two extra transport equations

$$\bar{\rho}\frac{Dk}{Dt} = \tau_{ij}\frac{\partial \tilde{w}_i}{\partial x_j} - \beta^* \bar{\rho} k \omega + \frac{\partial}{\partial x_j}\left(\mu + \sigma^* \mu_t\right)\frac{\partial k}{\partial x_j} \tag{11}$$

$$\bar{\rho}\frac{D\omega}{Dt} = \gamma \frac{\tau_{ij}}{\nu_t}\frac{\partial \tilde{w}_i}{\partial x_j} - \beta \bar{\rho}\omega^2 + \frac{\partial}{\partial x_j}\left(\mu + \sigma \mu_t\right)\frac{\partial \omega}{\partial x_j} + (1 - F_1)\,\bar{\rho}\frac{2\sigma_2}{\omega} \cdot \frac{\partial k}{\partial x_j} \cdot \frac{\partial \omega}{\partial x_j} \tag{12}$$

with β^*, σ^*, σ, γ, β, σ_2 another model constants. By the use of a function F_1, this model blends between the classical k–ε model in freestream regions and the k–ω model near the walls in fact. This blending function eliminates the boundary condition sensitivity.

On the right hand side of the energy equation an extra term $\overline{\rho w_i' h'}$ arises due to the averaging. This term represents turbulent transport of energy which is modelled regarding to the Boussinesq hypothesis as

$$\overline{\rho w_i' h'} = \frac{\mu_t}{\mathrm{Pr}_t}\frac{\partial \bar{h}}{\partial x_i}, \tag{13}$$

with $\mathrm{Pr}_t = 0.9$ the turbulent Prandtl number.

3. Mathematical Formulation and Boundary Conditions

After plugging turbulent transport equations (11) and (12) into the original set of equations (1) seven (resp. six) differential equations appear to be solved for 3D (resp. 2D) model. For the sake of clarity a 2D computational domain is shown and described in fig. 2. The solution of system (1), (11) and (12) is the function fulfiling *these equations* in the domain interior, *initial condition* at $t = 0$ and various *boundary conditions* (BC). In general four different BC's appear at each computation:

inlet mean value of velocity $\vec{w}_{inlet}$ is imposed through its magnitude and incidence angle, temperature $T = T_{inlet}$ and turbulent variables given by Menter's paper [3]

$$\begin{aligned} k &= k_{inlet} = \omega_{inlet} \cdot \frac{\mu_\infty}{100}, \\ \omega &= \omega_{inlet} = \frac{|\vec{w}_{inlet}|}{L_{ref}}. \end{aligned} \tag{14}$$

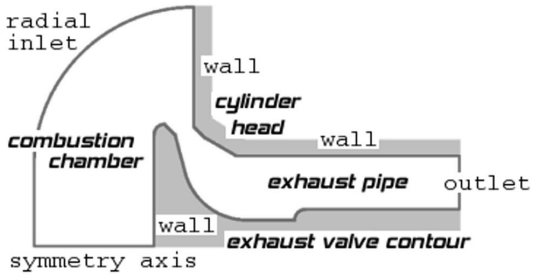

Fig. 2. Scheme of computational domain

outlet mean value of pressure p_{outlet} is imposed, such that pressure ratio over the domain reaches requested value.

symmetry axis so-called non-permeability condition $\vec{w} \cdot \vec{n} = 0$

wall so-called no-slip condition $\vec{w} = 0$ and for turbulent variables

$$\begin{aligned} k_{wall} &= 0 \\ \omega_{wall} &= \frac{60 \cdot \nu}{\beta_1 \cdot y_0^2} \end{aligned}$$

using again suggested expressions and parameters of the paper [3].

The inlet and outlet boundary conditions are completed by suitable Neumann's type conditions for remaining variables. Because the computational domain has been assumed symmetric along the valve axis, the 3D computations have been realized on a cylindrical wedge of the geometry. Therefore one more BC type appears for 3D computations:

cylindrical periodicity superposes variables from corresponding wedge surfaces.

4. Computational Grid

The computational domain has been covered with a computational grid, consisting of triangles and/or quadrilaterals for 2D computations (structured or unstructured configuration) and hexahedrons for 3D computations (only structured configuration). Fig. 3 shows examples of structured multi-block grids for planar and spatial cases. As hinted on the picture, the spatial grid has been constructed as an axisymmetric extrusion of the planar domain.

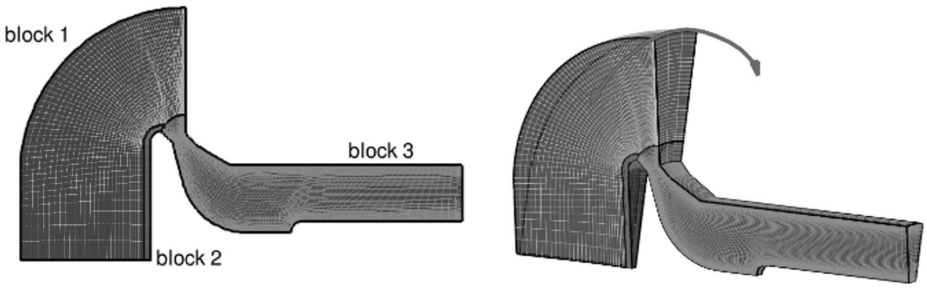

Fig. 3. Examples of structured multi-block grid, 2D – 3D

5. Numerical Method

The time marching method has been based on a Finite Volume Method (FVM). Hence the original set of equations (1) is discretized as

$$\frac{W_i^{n+1} - W_i^n}{\Delta t} = \frac{1}{\mu_i} \sum_{k=1}^{\#faces} \left(-\tilde{F}_k \cdot \vec{n}_k + \tilde{R}_k \cdot \vec{n}_k \right) , \tag{15}$$

with time derivative on the left-hand side, μ_i the meassure of i-th volume, $\tilde{F}_k$ the numerical approximation of advection fluxes F, G, H (see equation (18)), $\tilde{R}_k$ the numerical approximation of viscous fluxes R, S, T and $\vec{n} = (n_1,\, n_2,\, n_3)$ the unit outward normal vector to k-th face of the volume i.

5.1. Time Integration

Two methods of explicit or implicit time integration have been used. The explicit method evaluates the right-hand side of equation (15) at the time level n, allowing direct iterations in time. The implicit method computes fluxes from both the previous time level n and the actual time level $n + 1$, leading to a system of equations

$$W_i^{n+1} - W_i^n = \frac{\Delta t}{\mu_i} \sum_{k=1}^{\#faces} \left(-\tilde{F}\left(W^n,\, W^{n+1}\right)_k \cdot \vec{n}_k + \tilde{R}\left(W^n,\, W^{n+1}\right)_k \cdot \vec{n}_k \right) , \tag{16}$$

which transforms to

$$J\left(W^n\right) \cdot \Delta W = -R\left(W^n\right) , \tag{17}$$

with $J\left(W^n\right)$ the Jacobian matrix, $\Delta W = W^{n+1} - W^n$ the difference in the vector of unknowns and $R\left(W^n\right)$ the remaining terms (time dependent terms, numerical fluxes, source terms). Equation (17) has been solved by the GMRES iterative solver provided by PETSc (see [4]).

5.2. Advection Fluxes

A numerical scheme able to capture flowfields with wide velocity range was needed. Therefore the $AUSM^{+up}$ in a form of [5] has been used. The scheme is based on a solution of 1D Riemann problem (flux over a discontinuous step between two states W_L and W_R) and is extended to more space dimensions through rotation to the normal direction of the volume face. This approach converts any 2D or 3D fluxes to one dimensional case in fact. The numerical flux $\tilde{F}$ is then written

$$\tilde{F}_k \cdot \vec{n}_k = \frac{w_i \cdot n_i}{a} \cdot \begin{pmatrix} \rho a \\ \rho w_1 a \\ \rho w_2 a \\ \rho w_3 a \\ (\rho E + p)\, a \end{pmatrix} + \begin{pmatrix} 0 \\ n_1 \\ n_2 \\ n_3 \\ 0 \end{pmatrix} \cdot p \;\rightarrow = M_{LR} \cdot \Phi_{LR} + p_{LR} \tag{18}$$

with $a = \sqrt{\gamma \frac{p}{\rho}}$ the local speed of sound and $M_{LR} = \frac{\vec{w} \cdot \vec{n}}{a}$ the local Mach number in the normal direction. Terms M_{LR}, p_{LR} are computed with the splitting polynomials and Φ_{LR} is upwinded.

$$M_{LR} = \mathbf{M}^+_{(4)}(M_L) + \mathbf{M}^-_{(4)}(M_R) + \mathbf{M}_{corr} \tag{19}$$

$$p_{LR} = \mathbf{p}^+_{(5)}(p_L,\, M_L) + \mathbf{p}^-_{(5)}(p_R,\, M_R) + \mathbf{p}_{corr} \tag{20}$$

$$\Phi_{LR} = \begin{cases} \Phi\left(W_L\right) & \text{if } M_{LR} > 0 \\ \Phi\left(W_R\right) & \text{if } M_{LR} < 0 \end{cases} \tag{21}$$

Splitting polynomials are defined

$$\mathbf{M}^{\pm}_{(4)} = \begin{cases} \mathbf{M}^{\pm}_{(1)} & \text{if } |M| \geq 1 \\ \mathbf{M}^{\pm}_{(2)} \left(1 \mp 16 \cdot \beta \cdot \mathbf{M}^{\mp}_{(2)}\right) & \text{otherwise} \end{cases} \tag{22}$$

$$\mathbf{p}^{\pm}_{(5)} = \begin{cases} \frac{1}{M}\mathbf{M}^{\pm}_{(1)} & \text{if } |M| \geq 1 \\ \mathbf{M}^{\pm}_{(2)} \left[(\pm 2 - M) \mp 16 \cdot \alpha \cdot M \cdot \mathbf{M}^{\mp}_{(2)}\right] & \text{otherwise} \end{cases} \tag{23}$$

with lower order polynomials

$$\mathbf{M}^{\pm}_{(1)} = \frac{1}{2}\left(M \pm |M|\right), \qquad \mathbf{M}^{\pm}_{(2)} = \pm\frac{1}{4}\left(M \pm 1\right)^2. \tag{24}$$

Both equations (19), (20) contain correction terms, that ensure better convergence for low speed flows

$$\begin{aligned} \mathbf{M}_{corr} &= -\frac{K_p}{f_a} \max\left(1 - \sigma\bar{M}^2,\, 0\right) \cdot \frac{p_R - p_L}{\rho \cdot a^2} \\ \mathbf{p}_{corr} &= -K_u \cdot \mathbf{p}^{+} \cdot \mathbf{p}^{-} \cdot (\rho_L + \rho_R) \cdot f_a \cdot a \cdot (w_R - w_L) \end{aligned} \tag{25}$$

where

$$\begin{aligned} f_a = M_0\left(2 - M_0\right), \qquad \bar{M} = \frac{\sqrt{\frac{1}{2}w_L^2 + w_R^2}}{a_{LR}}, \\ M_0 = \min\left(1,\, \max\left(\bar{M},\, M_\infty\right)\right). \end{aligned} \tag{26}$$

M_∞ is a user-defined reference Mach number. The effect of correction terms (25) has been tested on an inviscid flow in planar channel with a 10 % circular arc bump on lower wall, so called GAMM channel [6].

Three flow regimes for $M_\infty = 0.675$, $M_\infty = 0.200$ and $M_\infty = 0.020$ have been tested by a numerical scheme without correction terms and with them respectively. The isolines of the Mach number are shown in fig. 4. An increase of robustness for a $AUSM^{+up}$ scheme has been observed, as the solution preserves better symmetry even for low and very low flow speeds, whereas the solution at nominal speed $M_\infty = 0.675$ remains untouched.

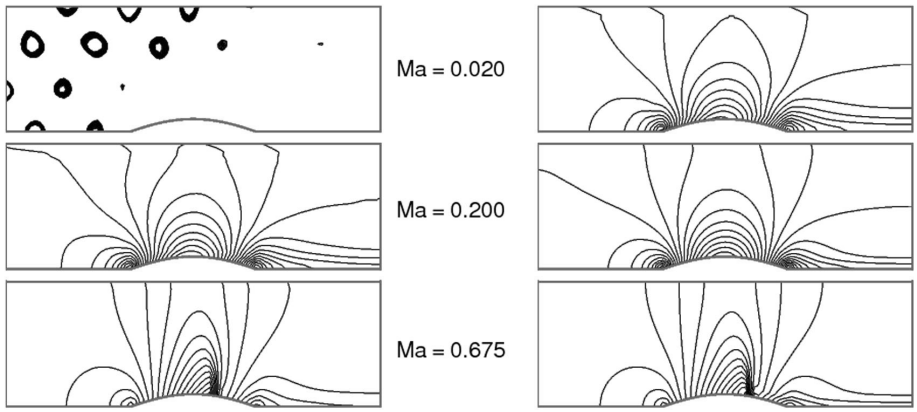

Fig. 4. Mach number isolines for AUSM scheme **without** correction terms (left) and **with** correction terms (right) for different main-stream velocity

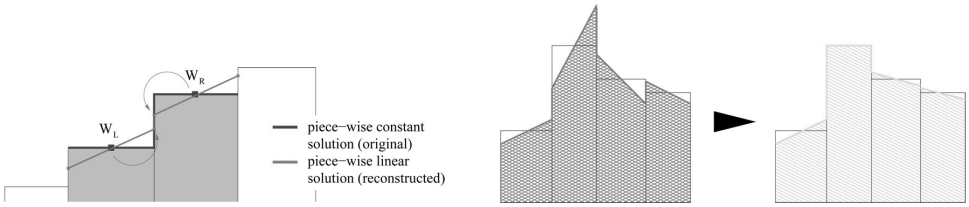

Fig. 5. Linear reconstruction of 1D solution (left), reconstructed values before and after a limiter application (right)

5.3. Viscous Fluxes

Viscous terms of equation (15) have been computed by a central approximation, using dual cells connecting neighbouring cell centroids with edge halves. The centroidal values have been given by the solution and the values at edge halves have been interpolated. Derivatives required for viscous fluxes (equation (3)) have been computed using the Green theorem.

6. Improvement of Spatial Accuracy

Spatial accuracy of upwind schemes is generally limited to first-order. For an improved accuracy the linear reconstruction with a limiter has been adopted in order to interpolate higher order left and right states across a cell interface, see fig. 5 left. Because the numerical scheme only requires values W_L and W_R without providing any information about their position and/or meaning the algorithm (18) remains unchanged also after the linear reconstruction.

Linear reconstruction might unfortunately lead to spurious oscilations (see fig. 5 right), hence a suitable limiter must always be applied in order to overcome convergence problems. This work shows results, which have used either the *minmod* [7] or the Barth limiter [8].

7. Results

7.1. Effect of the Numerical Scheme Accuracy

Fig. 6 presents a comparison of the first order scheme with the higher order solution. The figure presented has been obtained for 2D laminar flow model for valve opening 4 mm. The inlet flow temperature has been set to 500 K and pressure ratio $\frac{p_{inlet}}{p_{outlet}} = 4.0$.

The flow topology consists of a main beam, which accelerates from deep subsonic velocity in the combustion chamber to supersonic velocity at the exhaust pipe. The maximal Mach

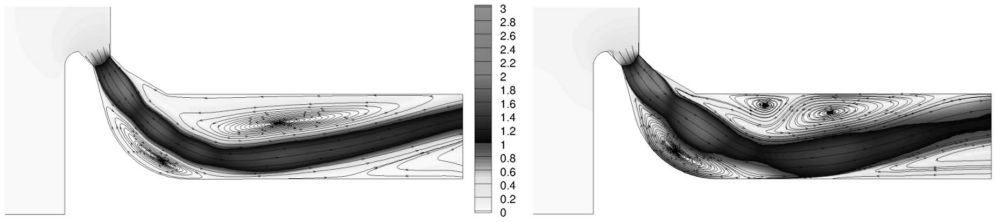

Fig. 6. Comparison 1st order solution (left), higher order solution (right), contours of Mach number, velocity streamlines

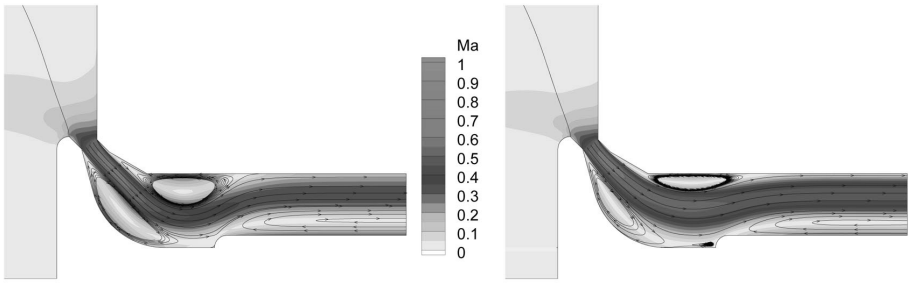

Fig. 7. Comparison 2D solution (left), planar slice of 3D solution (right), contours of Mach number, velocity streamlines

number reached within the flow is $M_{max} = 1.94$ for the first order solution and $M_{max} = 2.32$ for the higher order solution. The more accurate solution captures the expansion with better resolution and also the vortex structure around the beam shows more details. Only the higher order results are therefore shown on remaining figures of this paper.

7.2. Comparison of 2D and 3D Solution

Fig. 7 brings comparison of 2D and 3D solution. The results have been obtained for inviscid flow model with identical boundary conditions for both computations: valve opening 4 mm, inlet temperature 500 K, pressure ratio $\frac{p_{inlet}}{p_{outlet}} = 1.69$.

Even for these inviscid computations large recirculation zones have occured, also with one recirculation leaving and re-entering the outlet boundary for both cases. The impact of dimensionality is however indispensable in the velocity magnitude, size of recirculation zones and trajectory of the main flow beam.

7.3. Effect of the Valve Casing

Fig. 8 presents the influence of the detailness of the exhaust pipe. The results have been computed with a 2D laminar flow model, with the valve opening 4 mm, inlet temperature 500 K and the pressure ratio $\frac{p_{inlet}}{p_{outlet}} = 4.0$.

The casing strongly affects the recirculation zones on both sides of the channel. The smaller cross-section at the complete geometry (fig. 8, left) helps closing the separation along the upper wall and smoothes the exhaust in the pipe. The separation along the valve is larger on the other hand. The simplified geometry without casing (fig. 8, right) suffers from the backflow through the outlet boundary.

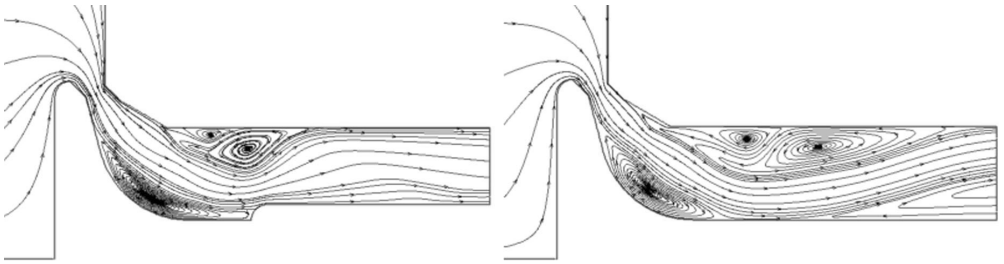

Fig. 8. Comparison of geometry with valve casing (left), without valve casing (right), velocity streamlines

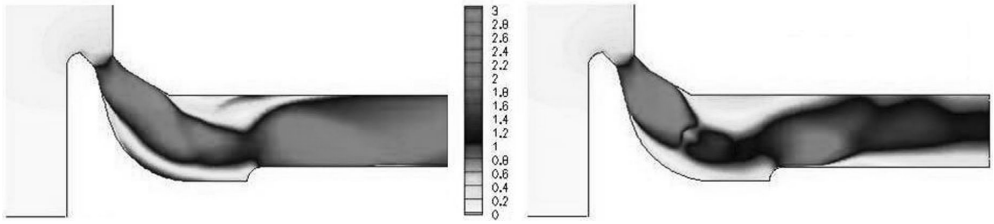

Fig. 9. Comparison of laminar (left) and turbulent (right) flow model, contours of Mach number

7.4. Influence of the Flow Model

The results in fig. 9 compare solutions for laminar and turbulent flow model at identical geometry and analogous boundary conditions: valve opening 4 mm, temperature 500 K, pressure at the inlet 400 kPa and at the outlet 100 kPa, analogically to the exhaust to the atmosphere.

Due to the additional dissipation of the turbulent flow model both the supersonic expansion and the recirculation zones are captured differently. The turbulent model does not allow such acceleration and its outlet is almost subsonic. The full structure is described in the following section.

8. Flow Structure

Fig. 10 reveals the flow topology of the turbulent solution. The result does not show any backflow through the outlet boundary and the average outlet velocity is $\bar{M}_{outlet} = 0.72$ (maximal outlet velocity $M_{outlet} = 1.12$). The overall maximal Mach number is $M_{max} = 2.85$ and appears inside the first supersonic expansion behind the seals.

Several separation zones have appeared in the domain due to the shock waves or the sharp corners. These separations form an artificial channel throat, which allows further expansion.

9. Conclusion

Several results of the gas exhaustion have been acquired with the new numerical code. The influence of particular factors such as the presence of the valve casing, dimensionality (2D or 3D model) and different flow model has been shown. The high sensitivity to these factors has been proved with even small modifications causing markant flow changes.

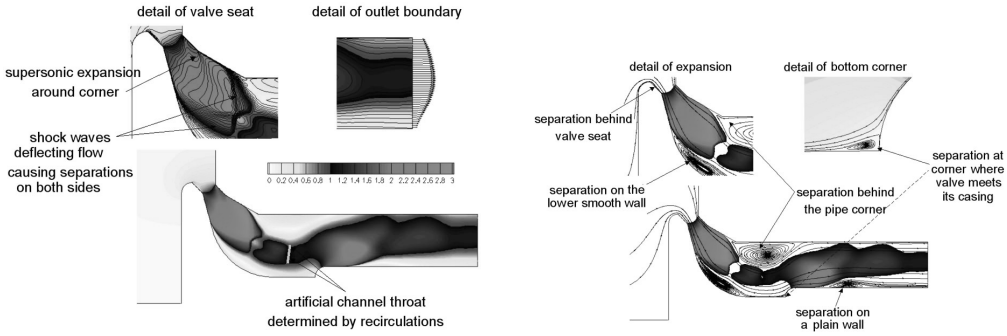

Fig. 10. Detailed flow structure of the turbulent solution

All results shown have contained several separation zones and their importance to the solution has been discovered. They have turned out to be the key issue in order to compute an accurate solution. Hence, the turbulent flow model seems to be the most appropriate. The turbulent result has therefore been explored in detail and it has shown more realistic features than the inviscid or laminar flow models.

Thus the turbulence model will be extended to 3D within the numerical code and also some further extensions of the code to unsteady boundary conditions and moving boundaries will be performed. Current work has shown that the gas exhaust is a complex phenomenon which does not allow many simplifications (dimension, shape, etc.) in order to obtain a trustworthy result.

Acknowledgements

This work has originated thanks to team of patient co-workers, grant of Czech Science Foundation No. P101/10/1329 and Josef Božek Research Center 1M6840770002.

References

[1] Favre, A., Équations des gaz turbulents compressibles, Journal de Mécanique 4, pp. 361–421, 1965.

[2] Menter, F. R., Rumsey, C. L., Assessment of two-equation turbulence models for transonic flows, AIAA Paper 94–2 343, 1994.

[3] Menter, F. R., Two-equation eddy-viscosity turbulence models for engineering applications, AIAA Journal, Vol. 32, pp. 269–289, 1994.

[4] Balay, S., Gropp, W. D., McInnes, L. C., Smith, B. F., Efficient management of parallelism in object oriented numerical software libraries, pp. 163–202, Birkhäuser Press, 1997.

[5] Liou, M. S., A sequel to AUSM, Part II: AUSM$^+$up for all speeds, Journal of Computational Physics 214, pp. 137–170, 2006.

[6] Ni, R. H., A multiple grid scheme for solving Euler equations, AIAA Journal, Vol. 20, pp. 257–264, 1981.

[7] LeVeque, R. J., Finite volume mehods for hyperbolic problems, Cambridge University Press, 2002.

[8] Barth, T. J., Jesperson, D. C., The design and application of upwind schemes on unstructured meshes, AIAA Paper 89–0366, 1989.